Journal of Laser Applications

Optimization and design for additive manufacturing of a fuel cell end plate

Cite as: J. Laser Appl. **34**, 042027 (2022); https://doi.org/10.2351/7.0000789
Submitted: 27 June 2022 • Accepted: 19 September 2022 • Published Online: 25 October 2022

Dirk Herzog, Tim Röver, Sagynysh Abdolov, et al.

Journal of Laser Applications ARTICLE scitation.org/journal/jla

Optimization and design for additive manufacturing of a fuel cell end plate

Cite as: J. Laser Appl. 34, 042027 (2022); doi: 10.2351/7.0000789
Submitted: 27 June 2022 · Accepted: 19 September 2022 ·
Published Online: 25 October 2022

Dirk Herzog,[1] Tim Röver,[1] Sagynysh Abdolov,[1] Florian Becker,[2] and Christoph Gentner[2]

AFFILIATIONS

[1]Institute of Laser and System Technologies (iLAS), Hamburg University of Technology (TUHH), Harburger Schloßstraße 28, 21079 Hamburg, Germany
[2]German Aerospace Center (DLR), Institute of Engineering Thermodynamics, Hein-Saß-Weg 22, 21129 Hamburg, Germany

Note: Paper published as part of the special topic on Proceedings of the International Congress of Applications of Lasers & Electro-Optics 2022.

ABSTRACT

Proton exchange membrane fuel cells (PEMFCs) represent today one of the most common types of fuel cells for mobility applications due to their comparatively high-power density, low operating temperature, and low costs. A PEMFC regularly consists of a stack of individual cells in which each consists of polar plates and a membrane electrode assembly. To achieve the best possible electric conductivity over the series connection of cells, the contact pressure in between the cells must be uniformly distributed over the cell area. This pressure is usually applied to the stack by end plates, which frame the stack and are clamped together by bolts, which are tightened by a defined torque. Typically, these end plates are made from bulk material with no or limited optimization. Looking at mobility applications, e.g., in aerospace, a fuel cell should ideally provide high efficiency at the lowest weight. Based on this assumption, this paper uses topology optimization varying the material as well as the design space to derive new design concepts for the end plates of a PEMFC. The designs are compared with respect to an even stress distribution to the fuel cell stack, the weight of the plates, and the manufacturability in the laser powder bed fusion process. The most promising design is manufactured and results in a weight decrease of 48% compared to previously used aluminum bulk plates. Finally, the optimized base plates are applied to a test cell and the performance is compared to their conventional counterparts, showing a 1% increase in electric stack power despite the lower mass.

Key words: design for additive manufacturing, fuel cell, laser powder bed fusion

I. INTRODUCTION

Hydrogen is today discussed as an energy carrier for mobile applications, e.g., for powering cars,[1] trucks, or airplanes.[2] Chemical energy from hydrogen may be transferred either into thermal energy by direct combustion or into electric energy using a fuel cell.[3] Among the different types of fuel cells, PEMFCs are commonly used due to their advantages, such as a high-power density of up to 2 kW/kg,[4] a low operating temperature of approximately 80 °C,[5] and comparatively low costs of 280 US$/kW.[6]

In a PEMFC, hydrogen is guided to the anode and oxygen to the cathode side of a membrane electrode assembly (MEA). At the anode, hydrogen is catalytically split into protons and electrons. While the protons permeate through the polymer electrolyte membrane, the electrons follow an external electric circuit to the cathode. There, the protons react with the oxygen molecules and the electrons to water molecules. A PEMFC is regularly built as a stack of cells, each of which consists of polar plates and an MEA. The MEA itself comprises the electrodes, the electrolyte, the catalyst, and the gas diffusion layers.[5] At each end of the PEMFC, an end plate is located and the assembly is fixated through bolts or a belt.[7]

Ideally, all cells of the assembly are at the same clamping pressure, and the pressure distribution is homogenous over the cross section.[8] Low pressure may result in too high electrical resistance between the gas diffusion layer and the bipolar plate,[9] whereas high pressure may result in a lack of permeability of the gas diffusion layer, which then negatively affects the efficiency.[10] Carral and

Mélé[11] modeled PEMFC stacks consisting of 2–16 cells and showed that deformation is usually highest at the cells facing the end plates, evening out toward the stack center. Thus, the end plates have an important function in PEMFCs by transferring the clamping loads from the bolts to the stack. To achieve an even pressure distribution, the end plates usually exhibit a bulk, rigid plate design, which, however, adds considerable weight to the PEMFC.

Dey *et al.*[12] modified the end plates and investigated three different geometric patterns. Each pattern was started on a regular plate design and was then extruded on top, and alternatively, the same pattern was cut out. The results showed that extrusion of a hexagonal structure leads to a more uniform pressure distribution. Additionally, Dey *et al.* also varied the number of bolts, showing that for their PEMFC design, the load distribution gets more even up to ten bolts. Additional bolts showed no further improvement. As materials, stainless steel 316, aluminum, and titanium were investigated, showing that changing the material affected the homogeneity of the load distribution to a lesser extent than the geometric patterns and the number of bolts. Aluminum was favored due to the lesser weight.

Lin *et al.*[13] also modified the end plates. To arrive at an optimized design, a topology optimization approach with two objectives was proposed: maximizing structural rigidity of the end plate and uniformizing the pressure distribution in the whole stack. The latter optimization goal was implemented by minimizing the root mean square of the displacements at all nodes in the contact area between the current collector and the equivalent stiffness block representing the stack. Both objectives are integrated into one objective function, applying individual weighting coefficients for each objective. They used an unspecified aluminum alloy for their investigations and implemented manufacturing restraints in order to be able to produce the resulting plate design by conventional manufacturing. Neither a value for weight saving was provided nor an experimental validation performed. Still, the work of Lin *et al.* shows the ability of topology optimization to derive complex weight optimized structures, which at the same time provide a homogenous pressure distribution.

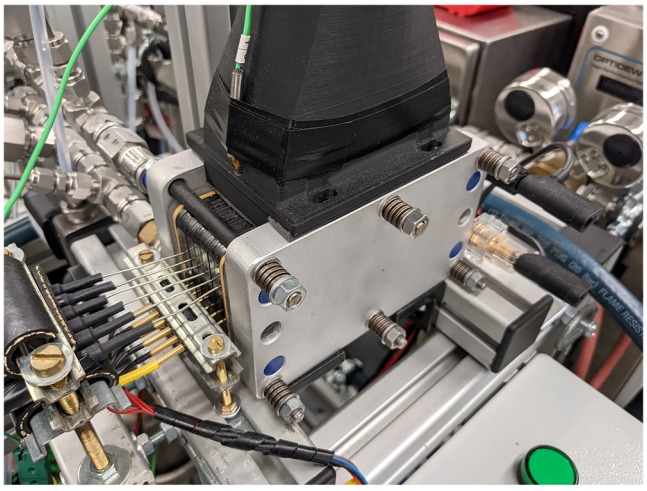

FIG. 1. Photograph of the PEMFC stack in an experimental setup with original end plates.

Additive manufacturing (AM) offers new design freedom allowing for the production of complex parts and geometries,[14] which are optimized for, e.g., light weight and functionality. The maturity of laser powder bed fusion (L-PBF) as a commonly used AM process today allows for the production of serial parts from a choice of engineering materials, including stainless steel, aluminum, and titanium,[15] making it a true alternative to other manufacturing routes. Thus, this paper investigates new designs for PEMFC end plates considering L-PBF as an option for the manufacturing.

II. METHODOLOGY

As a reference, the PEMFC stack shown in Fig. 1 was used. Geometrically, the original end plates have the outer dimensions of $140 \times 84 \times 15\ \text{mm}^3$ and consist of bulk aluminum. In the plate, a total of six holes of a diameter of 8 mm are present to allow for the bolts. Additionally, inlets and outlets for the reactants and products are integrated as well as screw holes for fixating an air cooler and fixation of the stack to the test stand. The weight of each plate is 435 g. To allow for an experimental comparison with the reference plates, all bore holes were kept as fixed and the number of bolts was not further optimized despite knowing from the work of Dey *et al.*[12] that an increase to ten bolts might be favorable, as discussed above.

The component optimization was conducted in two parts, namely, a preliminary and a final design study. In both studies, topology optimization simulations were carried out and then the resulting design concepts were investigated with respect to a homogeneous pressure distribution at the active area of the end plates by finite element analysis (FEA). The design studies investigate two different materials and a total of eight different design spaces.

A. Materials

As the exact alloy composition of the original end plates was not known, FEA of the original end plate was done considering AlSi10Mg as a material.

In the preliminary study, the two materials AlSi10Mg and Ti-6Al-4V were investigated. Both materials are well established in L-PBF and offer high lightweight potentials based on their mass-specific Young's moduli as well as tensile strength. Apart from that, AlSi10Mg was chosen as the conventional reference end plate is also from an aluminum alloy, and, therefore, FEAs of the original

TABLE I. Assumed properties of the selected materials.

Property/alloy	$AlSi_{10}Mg$	Ti-6Al-4V
Elastic modulus (GPa)	75	110
Poisson's ratio (—)	0.34	0.31[a]
Density (kg/m^3)	2.670	4.430
Yield strength (MPa)	260	1030
Tensile strength (MPa)	460	1150
Source	Refs. 16 and 17	Refs. 18–20

[a]Estimated value.

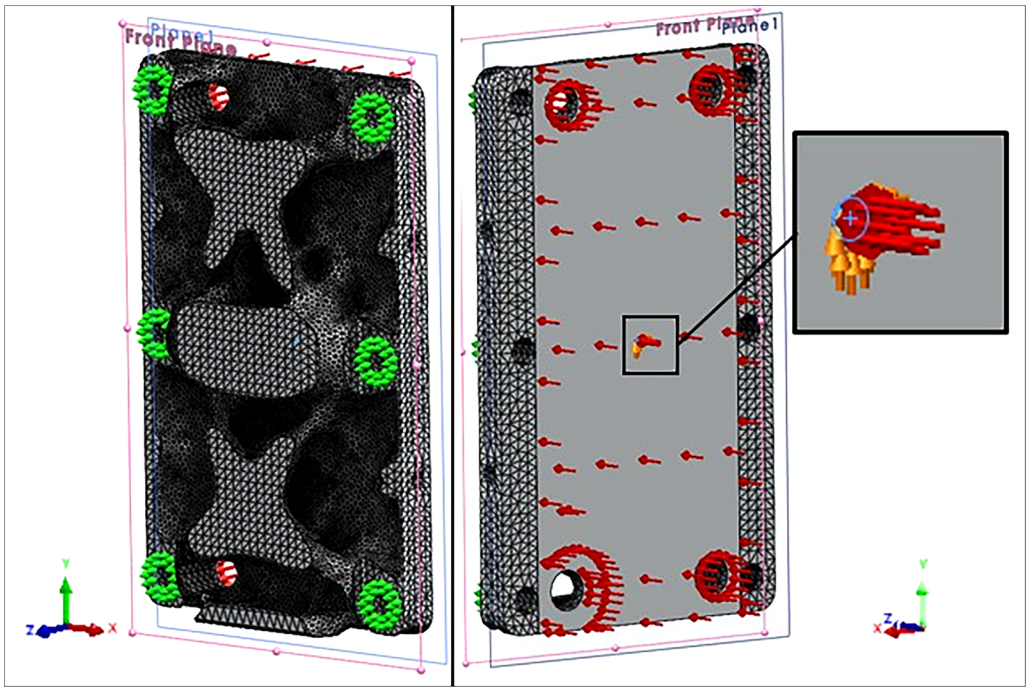

FIG. 2. Exemplary FEA (Al-10-pre) showing mechanical boundary conditions used for all topology optimizations and FEAs. Areas highlighted by green arrows are fixed in the z-direction. Areas highlighted by orange arrows are fixed in x- and y-directions. Areas highlighted by red arrows are subjected to pressure.

end plate design and the optimized $AlSi_{10}Mg$ end plate designs would allow a comparison regarding improvements due to geometric aspects of the designs.

Ti-6Al-4V was chosen as a material with similar weight-specific strength but at a higher density. It was expected that this fact would strongly influence the topology optimizations leading to different, presumably more compact designs. The properties for the materials were taken from the literature and are shown in Table I.

B. Mechanical boundary conditions

In the following, mechanical requirements of the end plates are presented that were introduced in the topology optimization models and the FEA-models.

The models were developed in such a way that the active areas of the end plates would lay in the x-y planes of the global coordinate systems, as shown in Fig. 2. The z-axes lay orthogonal to the x-y planes and, therefore, parallel to the acting directions of the pressures on the active areas of the end plates.

According to the assembly instructions of the used PEMFC test setup, the maximum torque value that could be applied to each of the six bolting connections was 2.0 Nm.

Based on the number of bolting connections (6), the applied torque for each bolting connection (2 Nm), the dimension of the nuts (M5), a k-value for normal dry connections (0.2), and the active area of the cell ($62.6 \times 137.6\,mm^2$), the calculated pressure load on the active area of the cell was calculated as 0.12 MPa. This pressure was assumed to act on the active area of the end plates (i.e., the area transmitting the loads to the stack).

Furthermore, the contact surfaces of the nuts were modeled as circular rings on the end plates. They were fixed in the z-direction, as the bolting connections prevent any considerable deformation in this direction.

To develop fully determined mechanical models, small cylindrical extrusions with a diameter of 1 mm and a height of 0.1 μm were added to each of the models at the center of the active area of the end plates as auxiliary features of the optimizations. The curved surface of these auxiliary features was fixed in the x-y plane.

Furthermore, some volumes of the design space were excluded from the optimization by defining them as preserved regions.

The bottom surface of the end plate can be divided into the active area of the end plate and the remainder of the bottom surface. A layer of 1 mm was added to the remainder of the bottom surface as a preserved region.

Furthermore, a layer of 1 mm of the preserved region was added to one of the surfaces at the side of the end plate in which the threads are to be produced. A layer of 2 mm of the preserved region was added to the surfaces at the other side of the end plate in which other threads are to be manufactured. Other than that, all six holes for the bolting connections were preserved at the curved surfaces up to 1 mm in the radial direction. The holes for all four threads were preserved at the curved surfaces up to 2 mm in the radial direction.

TABLE II. Overview over investigated combinations between material and design space for a preliminary design study.

Study type	Material	Thickness at bolting connections (mm)	Thickness of extrusion (mm)
Ti-0-pre	Ti-6Al-4V	8	0
Ti-7-pre	Ti-6Al-4V	8	7
Al-0-pre	$AlSi_{10}Mg$	10	0
Al-5-pre	$AlSi_{10}Mg$	10	5
Al-10-pre	$AlSi_{10}Mg$	10	10
Al-15-pre	$AlSi_{10}Mg$	10	15
Al-20-pre	$AlSi_{10}Mg$	10	20
Al-30-pre	$AlSi_{10}Mg$	10	30

C. Topology optimization

A solid isotropic material with penalization method (SIMP) approach was used for the topology optimizations in this work.[21] This approach is the most widely used one in the literature due to its robustness and computational efficiency. Furthermore, the choice of SIMP allows for comparison of the results with previous studies, such as presented in Ref. 13.

Objectives of the optimization were mass reduction and minimization of the compliance of the structure. For more details of the objective function as implemented in this study, the reader is kindly referred to Ref. 21. To consider material costs as an additional objective with costs of Ti-6Al-4V being higher than those of $AlSi_{10}Mg$, the mass objectives were defined as 240 and 210 g for optimizations of $AlSi_{10}Mg$ and Ti-6Al-4V, respectively. Tetrahedral elements were used for discretization in the topology optimizations because robust automatic meshing algorithms can be used with this element type. The mesh sizes for the topology optimizations are stated in Table III. No manufacturing constraints were implemented in the topology optimization algorithm. Instead, the topology optimization results were manually assessed and adapted for manufacture by L-PBF (also cf. Sec. V).

D. Evaluation of a homogeneous pressure distribution

A homogeneous pressure distribution in the active area of the end plates was evaluated indirectly with the help of FEA. The difference between maximum displacement in the z-direction and minimum displacement in the z-direction within the active area of the end plate (Δz_{AA}) was evaluated as a measure of a homogeneous pressure distribution in the active area of the end plate under load. Same as for the topology optimization, tetrahedral elements were used for discretization in the FEAs. For the FEA of study type, the mesh sizes that were preselected by the software SOLIDWORKS 2019–2020 were used with values for the mesh sizes ranging between 4.2 and 4.7.

E. Software

SOLIDWORKS 2019–2020 was used for topology optimizations and FEAs in this work.

III. PRELIMINARY DESIGN STUDY

In the preliminary study, eight combinations (study types) between the two materials and different design spaces were defined and investigated to identify the most promising combination for the final design study. In Table II, relevant data for all eight combinations are stated. Design spaces consist of two parts: A base part that has a thickness of 8 mm (Ti-6Al-4V) and 10 mm ($AlSi_{10}Mg$) and an extrusion that has a thickness between 0 and 30 mm. All design spaces are depicted in Fig. 3.

At the boltings, the thickness of the plate was fixed to a value lower than in the original bulk plate. On the one hand, a low thickness is advantageous so that the volume of preserved regions stays low. On the other hand, too low values might lead to stress peaks. Therefore, suitable values for the thickness of these regions were estimated as 8 mm for titanium and 10 mm for aluminum, taking the higher Young's modulus of titanium into account. A separate study would be needed to optimize the thickness in the bolting region if further mass savings are desired.

In Fig. 3, results of the topology optimizations of the preliminary study can be found. It can be seen that only for the aluminum designs, complex geometrical shapes were generated. Considering

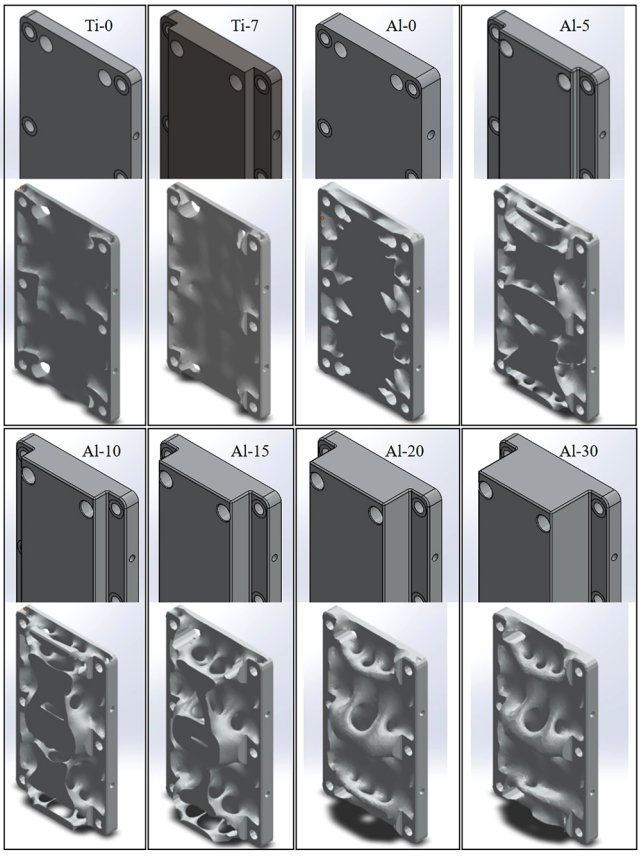

FIG. 3. Overview of design spaces and topology optimization results of the eight cases that were investigated in the preliminary study.

the aluminum type optimizations, only for optimizations of types Al-20 and Al-30, the extrusions were large enough such that no material was placed at the boundary of the extrusion facing away from the active area of the end plate. Therefore, these two samples did not seem to be "cut off" at the end of the extrusion area.

The designs that were developed with the help of topology optimizations were then evaluated by FEA by applying the same mechanical boundary conditions to all of the designs, as discussed in Sec. II. Figure 4 shows the applied evaluation of minimum and maximum displacements in the z-direction in the active area of the end plate for an exemplary design. Additionally, Table III states information about the maximum occurring von Mises stresses, masses, and differences between the maximum displacement in the z-direction and the minimum displacement in the z-direction within the active area of each end plate (Δz_{AA}) for all combinations that were investigated in a preliminary study.

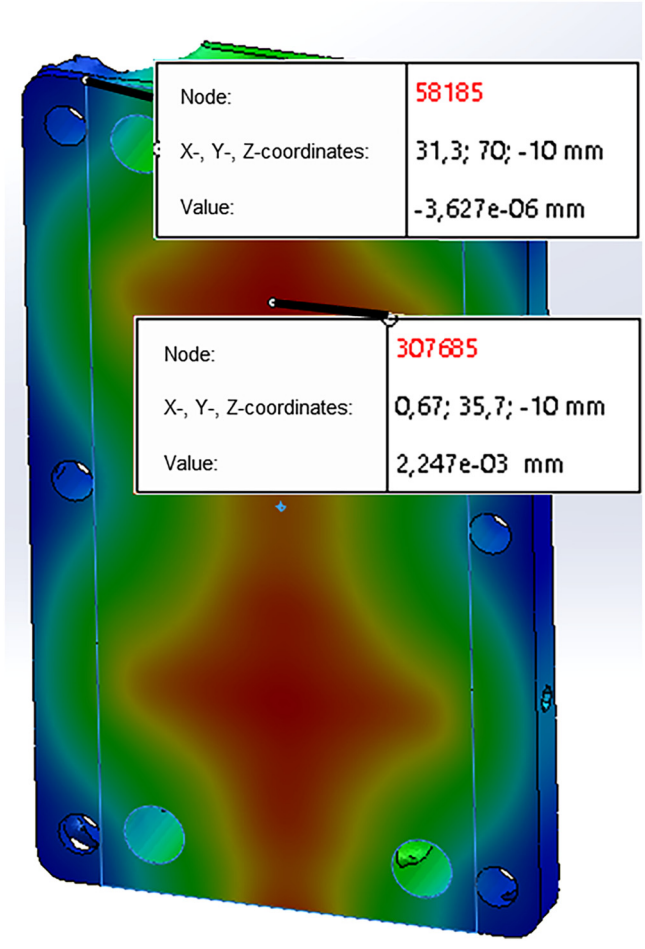

FIG. 4. Screenshot of evaluation by FEA of minimum and maximum displacements in the z-direction in an active area of the end plate for the final end plate design (Al-10-fin). The active area of the endplate is given by a highlighted rectangle.

Considering results from the preliminary study, Table II, it can be seen that the displacement Δz_{AA} decreases with increasing extrusion up to 10 mm, as finer, more complex bridgelike structures develop in the extruded area (also cf. Fig. 3). Surprisingly, a further increase in extrusion led to higher displacements. It should be noted that this might be a result of the mesh size, which had to be increased proportional to the extrusion for reasons of limited computational capacity when performing the preliminary study.

As Al-10 performed best in terms of Δz_{AA} and should, thus, provide a homogenous pressure distribution in the active area, this study type was used as a starting point for the final design study.

IV. FINAL DESIGN STUDY

For development of the final design study, a system with higher computational capacity was used, thus allowing for finer meshes in both topology optimization and FEA.

Table III states FEA results of the original plate, the preliminary study, and the final study. The thickness of the original plate was 15 mm. Comparing results of study types Al-10-pre and Al-10-fin, that only differed in the used mesh sizes, it can be seen that Al-10-fin yielded better results in terms of maximum occurring von Mises stresses, mass, and Δz_{AA}. Comparing Al-10-fin and Al-Or, it was observed that the mass could be reduced by approximately 48%. However, FEA suggests that Al-10-fin has a higher Δz_{AA} than Al-Or, which was expected to lead to a worse pressure distribution and, therefore, to a worse performance of the fuel stack in application.

V. ADDITIVE MANUFACTURING AND POSTPROCESSING

The final design was checked and adapted for manufacturability by L-PBF, keeping to the design limits for $AlSi_{10}Mg$, which includes a minimum wall thickness of 0.5 mm, and supports are added for all surfaces with angles below 45° toward the build plate, as suggested by Atzeni and Salmi.[22] At the contact surface of the end plate, a 1.5 mm layer of the material was added to the design to ensure that machining is possible after AM. The machining step was foreseen in order to obtain a plane contact surface and to remove any warpage from residual stresses as well as excessive surface roughness.

The printing of the two end plates was then performed at Franken Guss GmbH & Co. KG, Kitzingen, Germany. Part orientation was chosen in order to avoid excessive supports in the central area of the plate, where support removal was assumed to be most complex, and reduce residual stresses; cf. Fig. 5. Figure 6 shows the end plate prior to removal of all support structures. After printing, the supports were removed manually, followed by milling of the contact surface. The machining was done such that the final material thickness at all six boreholes (for the bolts) was 10 mm. The boreholes for the bolting connections were not postprocessed. The four boreholes for the fluid connections were intentionally undersized in the computer-aided design (CAD)-file to enable exact postprocessing. The four boreholes were machined such that a final diameter of 10 mm was achieved. It was found that the distance between the boreholes was slightly different from the original CAD-file, which was assumed to be due to a certain warp of the AM-component. The final weight of the two end plates manufactured this way was 221.68 and 221.24 g for plates 1 and 2,

TABLE III. Maximum occurring von Mises stresses, mesh size of topology optimizations (TOs), masses, and differences between maximum displacement in the z-direction, and minimum displacement in the z-direction within the active area of each end plate (Δz_{AA}) based on FEAs for all study types.

Study type	Maximum von Mises stress (MPa)	Mesh size in TOs (mm)	Mass of design (g)	Δz_{AA} (mm)
Comparison study (original plate, thickness: 15 mm)				
Al-Or-pre	6.8	3	435	1.38×10^{-3}
Preliminary study				
Ti-0-pre	124.8	1.96	204	1.72×10^{-2}
Ti-7-pre	440.7	2.4	216	1.64×10^{-2}
Al-0-pre	44.0	2.1	240	4.03×10^{-3}
Al-5-pre	74.3	2.3	238	3.00×10^{-3}
Al-10-pre	37.5	2.5	232	2.91×10^{-3}
Al-15-pre	30.3	2.6	234	3.46×10^{-3}
Al-20-pre	59.0	2.8	242	3.76×10^{-3}
Al-30-pre	59.3	3	240	4.07×10^{-3}
Final design study				
Al-10-fin	34.5	1.5	226	2.25×10^{-3}

respectively. The PEMFC stack assembled with the two optimized end plates is depicted in Fig. 7.

VI. EXPERIMENTAL CHARACTERIZATION

For the experimental characterization of the optimized end-plates, a 100 W air-cooled PEMFC stack manufactured by ZBT GmbH was used. The stack consists of five individual cells with a respective electrochemical surface area of 50 cm^2.

A. Experimental setup

The schematic drawing of the experimental setup is depicted in Fig. 8.

The gas supply of pressurized hydrogen and air is regulated by two mass flow controllers (MFCs). The two gases are humidified by membrane humidifiers combined with a heat bath with a constant operating temperature of 35 °C. To control the humidity of the supplied air at the cathode inlet of the stack to a fixed value of 85%, a bypass valve is used.

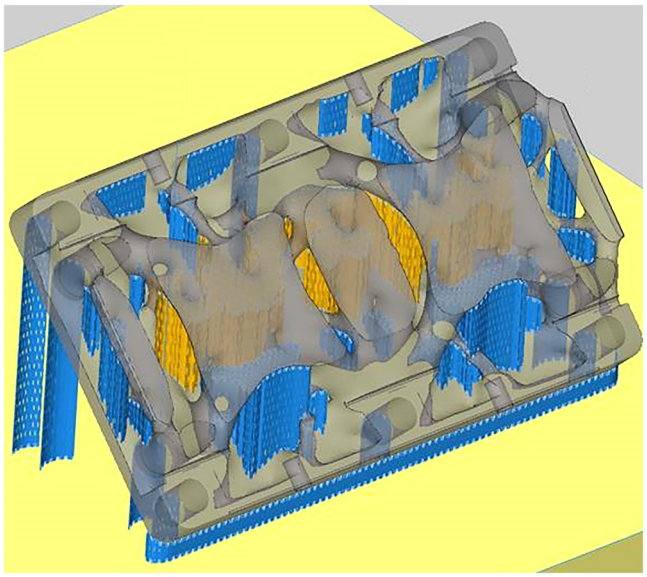

FIG. 5. Screenshot of a prepared AM-build job showing support structures that are difficult to access with tools (orange) and support structures that are easy to access with tools (blue).

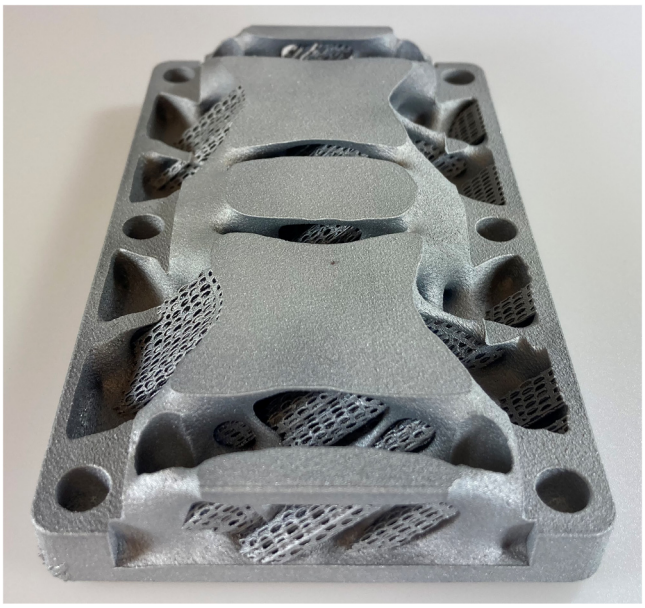

FIG. 6. Photograph of an additively manufactured end plate prior to removal of remaining support structures.

FIG. 7. Photograph of the PEMFC stack assembly with two optimized additively manufactured end plates.

On the anode side, a membrane pump is implemented to feed back the residual hydrogen to the anode inlet of the stack. This is done to increase the flow rate of hydrogen through the stack and, thus, its stoichiometric ratio of hydrogen, which results in a more homogeneous gas, humidity, and temperature distribution. Furthermore, a solenoid valve is integrated in the purge line of the anode system in order to control the removal of diffused water and nitrogen from the cathode to the anode side.

The temperature regulation at the cooling outlet of the stack is done by an axial blower, which sucks air from the environment through the stack. It should be noted that suction of air allows a more even flow into the cooling channels compared to blowing, leading to a more even temperature and voltage distribution of the stack.

To control the electric power output of the stack, a thermal DC-load (EA-EL 9000T) is used, which allows a maximum electric power of 600 W and an electric current of up to 45 A.

B. Experimental procedure

For the experimental investigation, two procedures were chosen, where the stack is operated according to the data sheet of the stack[23] in a galvanostatic (control of electric current) mode. The first procedure is used for the precondition of the stack, which combines static and dynamic operation of the stack in a medium load range to ensure the reproducibility of the measurement results. The second procedure is used to characterize the stack to determine its polarization curve and power curve (VI-PI-curve). Both procedures are shown in Fig. 9.

The VI-curve procedure starts without interruption after the conditioning procedure. Here, the electric current is stepwise increased to 45 A and afterward stepwise decreased to 3.5 A. Each stage is held for 5 min. These two procedures are repeated during the following three test phases of the experimental investigation:

Phase 1:

- Assemble the stack with the original end plates according to the instructions of the manufacturer.[24]
- Five new cells are used in order to exclude the influence of existing degradation and previous operation.
- Repeat the conditioning and VI-curve procedure until the measured cell voltages of the VI-curves are comparable.

Phase 2:

- Assemble the stack with the optimized end plates according to the instructions of the manufacturer.
- Keep the five cells from phase 1.
- Repeat the conditioning and VI-curve procedure until the measured cell voltages of the VI-curves are comparable.

Phase 3:

- Assemble the stack with the original end plates according to the instructions of the manufacturer.
- Keep the five cells from phase 2.
- Execute the conditioning and VI-curve procedure to get a final reference.

C. Experimental results and discussion

For the evaluation of the VI-curve procedure, the measured stack voltage of each stage from 45 to 3.5 A is averaged over the last 60 s per stage. The results of test phase 1 are shown in Fig. 10.

As expected, the lowest voltages were measured at the first VI-curve (test no. 1). This is related to the new cells, which are initially dry and, thus, have a relatively high membrane resistance. Furthermore, impurities of the carbon carrier from the manufacturing process prevent the entire electrochemical surface area (ECSA) from being used, which results in a limited cell potential.

With the help of the repeated conditioning- and VI-curve procedure, the cell membranes get humidified and the initial impurities of the carbon carrier are dissolved. Subsequently, the measured cell voltages increase until the maximum ECSA is available. At test no. 8, a lower cell voltage was measured compared to test no. 7. The maximum cell voltage was measured at test no. 11. Thus, an average value of test nos. 8–12 was calculated, which results in a reference VI-curve for the second test phase.

In test phase 2, the conditioning- and VI-curve procedure was repeated 13 times with the optimized end plates. The results are shown in Fig. 11. The individual values per test nos. 13–25 in the figure are provided without further differentiation in color with the intention to show the variance of the data only.

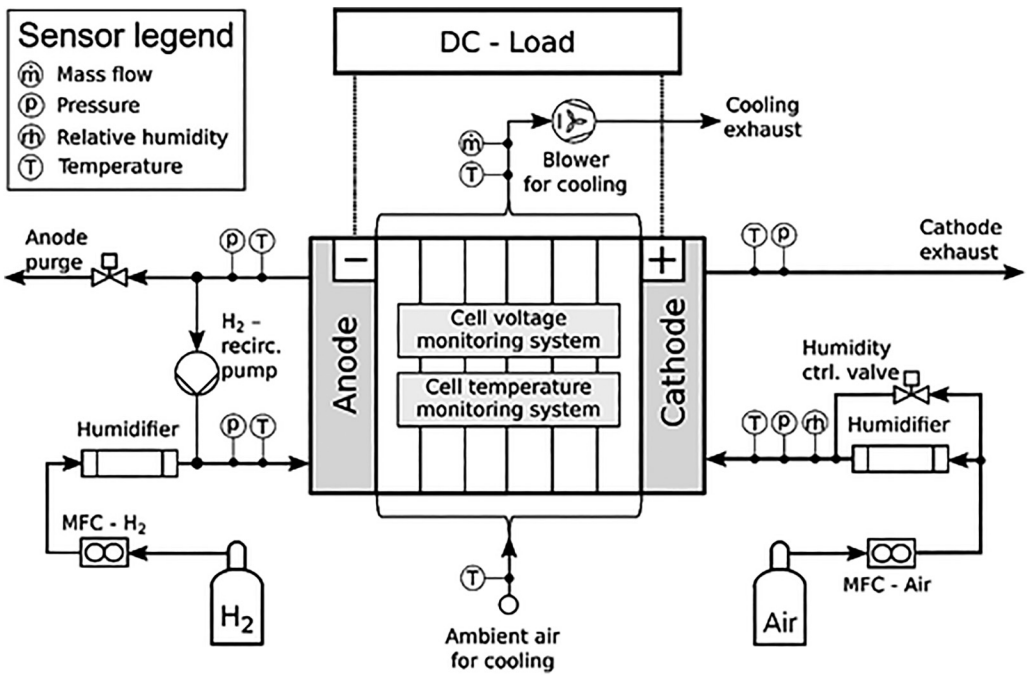

FIG. 8. Schematic drawing of an experimental setup.

It can be seen that all VI- and PI-curves measured with the optimized end plates result in a higher voltage and power in the upper current region compared to the reference curve from test phase 1.

A closer look into the upper current region is shown in Fig. 12. Here, the resulting VI- and PI-curve from test phase 3 (test no. 26) is depicted as well. It should be noted that test phase 3 was carried out directly after test phase 2 in order to exclude influences on the cell condition due to a longer standing time.

In test phase 2, the maximum electric stack power of 107.8 W @45 A was obtained in test no. 17 and the minimum stack power of 105.2 W @45 A in test no. 23. This corresponds to a variation of the average cell voltage of 12 mV in the measurements of test phase 2. This variation is related to a slightly variable ambient temperature and standing times as the measurements were conducted on 15 different days.

In test phase 2, an average electric stack power of 105.9 W @45 A was obtained within 13 tests. Compared to the reference curve from test phase 1, with a maximum electric stack power of 104.8 W @43.8 A, an increase of 1.1 W was achieved. Accordingly, an improved stack performance of about 1% was achieved with the optimized end plates.

Thus, the effect of stiffer end plates for a more even stress distribution of the cells on the resulting stack performance is relatively

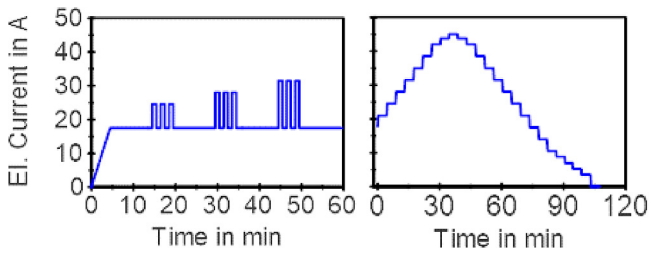

FIG. 9. Experimental procedures (left: conditioning, right: VI-PI-curve).

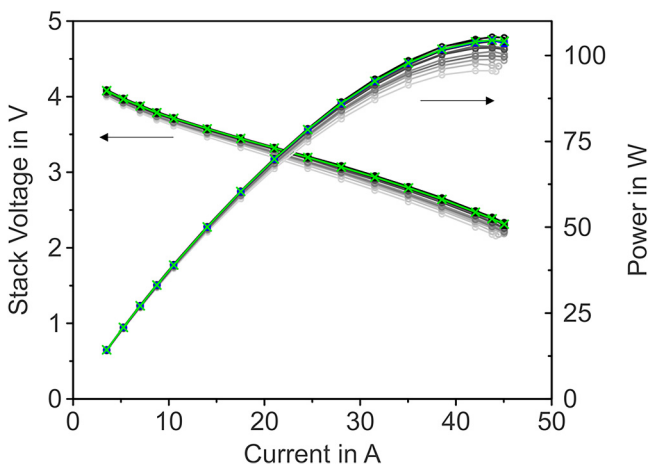

FIG. 10. VI-PI-curves of test phase 1 (original end plates).

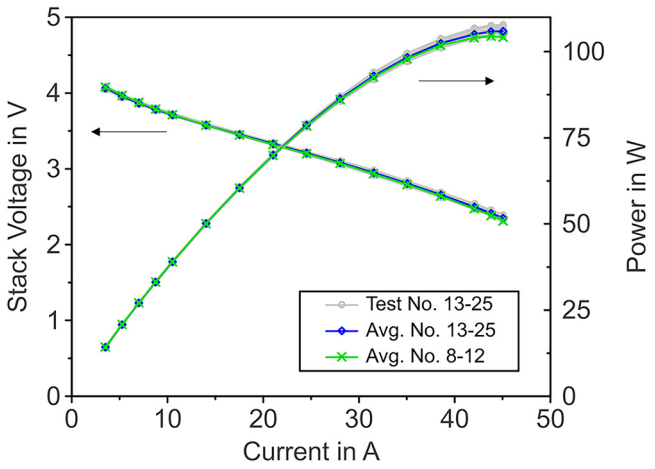

FIG. 11. VI-PI-curves of test phases 1 and 2 and comparison with an average value of test phase 1.

low. As the cell area of 50 cm^2 is quite small compared to commercial fuel cell stacks for, e.g., mobile applications, it is assumed that a higher improvement of the stack performance can be achieved when stacks with a larger cell area are used.

The VI- and PI-curve of test no. 26, where the original end plates were used again, is comparable to the reference curves from test phase 1. This supports the assumption that the presented results are reproducible.

VII. SUMMARY AND OUTLOOK

End plates of a PEMFC stack were optimized by weight and a homogenous pressure distribution using a topology optimization approach. It was shown that extruding the boundary box by 10 mm leads to the generation of fine, bridgelike structures that can effectively transfer the forces from the bolts to the active area of the stack. Using such a design and manufacturing it in L-PBF from $AlSi_{10}Mg$ reduced the mass of the component by 49%. The optimized end plates were applied to a regular PEMFC stack with a cell area of 50 cm^2, and their performance was compared to the original end plates, yielding an approximate performance increase of 1%.

For stacks with a larger cell area, higher improvements may be expected.

The slight increase in performance was observed experimentally; despite that, in the FEA, the new design was not able to improve the displacement values in the active area. A further theoretical analysis is planned to better understand the parametric correlation between the surface area, end plate designs, and plate stiffness.

Furthermore, end plate optimization would also allow for extension of the functionality of the end plates, especially in terms of the thermal management of the stack to achieve a more even temperature distribution across the stack or support the cold start behavior of a fuel cell system.

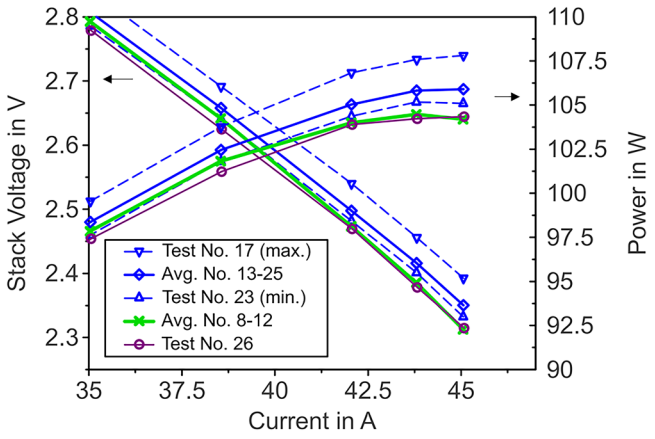

FIG. 12. VI-PI-curves of test phases 1–3.

ACKNOWLEDGMENTS

The authors would like to express their gratitude to the company Franken Guss GmbH & Co. KG for the support and discussion of the printing of the end plates. Furthermore, the authors would like to thank Anna Vorndran (DLR) for carrying out the experimental campaign.

AUTHOR DECLARATIONS

Conflict of Interest

The authors have no conflicts to disclose.

Author Contributions

Dirk Herzog: Conceptualization (equal); Methodology (equal); Supervision (equal); Writing – original draft (equal); Writing – review & editing (equal). **Tim Röver:** Conceptualization (equal); Methodology (equal); Writing – original draft (lead); Writing – review & editing (equal). **Sagynysh Abdolov:** Investigation (lead); Methodology (lead); Validation (lead); Writing – original draft (supporting). **Florian Becker:** Methodology (equal); Validation (equal); Writing – original draft (equal); Writing – review & editing (equal). **Christoph Gentner:** Methodology (equal); Validation (equal); Writing – original draft (equal); Writing – review & editing (equal).

REFERENCES

[1]M. A. Rosen and S. Koohi-Fayegh, "The prospects for hydrogen as an energy carrier: An overview of hydrogen energy and hydrogen energy systems," Energy Ecol. Environ. **1**, 10–29 (2016).
[2]A. Baroutaji, T. Wilberforce, M. Ramadan, and A. G. Olabi, "Comprehensive investigation on hydrogen and fuel cell technology in the aviation and aerospace sectors," Renew. Sustain. Energy Rev. **106**, 31–40 (2019).
[3]S. S. Ravi and M. Aziz, "Clean hydrogen for mobility—Quo vadis?," Int. J. Hydrogen Energy **47**, 20632–20661 (2022).
[4]M. Moein Jahromi and H. Heidary, "Automotive applications of PEM technology," in *PEM Fuel Cells* (Elsevier, Amsterdam, 2021), pp. 347–405.

[5]P. Sharma and O. P. Pandey, "Proton exchange membrane fuel cells: Fundamentals, advanced technologies, and practical applications," in *PEM Fuel Cells* (Elsevier, Amsterdam, 2021), pp. 1–24.
[6]G. Kaur *et al.*, "Economic, business, technical, and commercialization hindrances for the polymer electrolyte membrane fuel cell," in *PEM Fuel Cells* (Elsevier, Amsterdam, 2021), pp. 407–427.
[7]C. W. Wu, W. Zhang, X. Han, Y. X. Zhang, and G. J. Ma, "A systematic review for structure optimization and clamping load design of large proton exchange membrane fuel cell stack," J. Power Sources **476**, 228724 (2020).
[8]S. Karvonen, *Modelling Approaches to Mass Transfer and Compression Effects in Polymer Electrolyte Fuel Cells* (VTT, Espoo, 2011).
[9]P. Zhou, C. W. Wu, and G. J. Ma, "Contact resistance prediction and structure optimization of bipolar plates," J. Power Sources **159**, 1115–1122 (2006).
[10]M. Habibnia, M. Shakeri, S. Nourouzi, and P. G. Tamami, "Investigation and optimization of a PEM fuel cell's electrical and mechanical behavior," Iran. J. Hydrogen Fuel Cell **3**, 1–10 (2016).
[11]C. Carral and P. Mélé, "A numerical analysis of PEMFC stack assembly through a 3D finite element model," Int. J. Hydrogen Energy **39**, 4516–4530 (2014).
[12]T. Dey, J. Deshpande, D. Singdeo, and P. C. Ghosh, "Study of PEM fuel cell end plate design by structural analysis based on contact pressure," J. Energy **2019**, 3821082.
[13]P. Lin, P. Zhou, and C. W. Wu, "Multi-objective topology optimization of end plates of proton exchange membrane fuel cell stacks," J. Power Sources **196**, 1222–1228 (2011).
[14]C. Klahn, B. Leutenecker, and M. Meboldt, "Design strategies for the process of additive manufacturing," Proc. CIRP **36**, 230–235 (2015).
[15]D. Herzog, V. Seyda, E. Wycisk, and C. Emmelmann, "Additive manufacturing of metals," Acta Mater. **117**, 371–392 (2016).
[16]EOS GmbH, "EOS aluminum $AlSi_{10}Mg$: Material data sheet," see https://www.eos.info/de/additive-fertigung/3d-druck-metall/eos-metall-werkstoffe-dmls/aluminium-3d-druck (accessed June 1, 2022).
[17]E. Sert, L. Hitzler, S. Hafenstein, M. Merkel, E. Werner, and A. Öchsner, "Tensile and compressive behaviour of additively manufactured $AlSi_{10}Mg$ samples," Prog. Addit. Manuf. **5**, 305–313 (2020).
[18]EOS GmbH, "EOS titanium Ti_{64}: Material data sheet," see https://www.eos.info/03_system-related-assets/material-related-contents/metal-materials-and-examples/metal-material-datasheet/titan/ti64/ti-ti64-m280-m290-400w_material_data_sheet_05-14_en.pdf (accessed June 1, 2022).
[19]ASM International, *Properties and Selection Nonferrous Alloys and Special-Purpose Materials*, 10th ed. (American Society for Metals, Metals Park, OH, 1990).
[20]L. Facchini, E. Magalini, P. Robotti, A. Molinari, S. Höges, and K. Wissenbach, "Ductility of a Ti-6Al-4V alloy produced by selective laser melting of prealloyed powders," Rapid Prototyp. J. **16**, 450–459 (2010).
[21]Dassault Systèmes, "SIMP method for topology optimization—2020—SOLIDWORKS help," see https://help.solidworks.com/2020/English/SolidWorks/cworks/c_simp_method_topology.htm (accessed June 21, 2022).
[22]E. Atzeni and A. Salmi, "Study on unsupported overhangs of $AlSi_{10}Mg$ parts processed by direct metal laser sintering (DMLS)," J. Manuf. Process. **20**, 500–506 (2015).
[23]Zentrum für Brennstoffzellen Technik ZBT GmbH, *Specification Typical Stack Data ZBT FC Stacks: PEM-FC-Stack 24 Cells (Hydrogen)*.
[24]Zentrum für Brennstoffzellen Technik ZBT GmbH, *Montageanleitung, Brennstoffzellenstack, Mai 2012—Projekt: DLR 39000: Revision 20120514, RBS.*